Check for updates

Journal of
Materials Chemistry A

Accepted Manuscript

Volume 4 | Number 1 | 7 January 2016 | Pages 1–330

Journal of
Materials Chemistry A

Materials for energy and sustainability
www.rsc.org/MaterialsA

ISSN 2050-7488

ROYAL SOCIETY OF CHEMISTRY

PAPER
Kun Chang, Zhaorong Chang et al.
Bubble-template-assisted synthesis of hollow fullerene-like
MoS₂ nanocages as a lithium ion battery anode material

175 YEARS

This is an Accepted Manuscript, which has been through the Royal Society of Chemistry peer review process and has been accepted for publication.

Accepted Manuscripts are published online shortly after acceptance, before technical editing, formatting and proof reading. Using this free service, authors can make their results available to the community, in citable form, before we publish the edited article. We will replace this Accepted Manuscript with the edited and formatted Advance Article as soon as it is available.

You can find more information about Accepted Manuscripts in the author guidelines.

ROYAL SOCIETY OF CHEMISTRY

rsc.li/materials-a

Journal of Materials Chemistry A

PAPER

In-Situ g-C₃N₄ Self-Sacrificial Synthesis of g-C₃N₄/LaCO₃OH Heterostructure with Booming Interfacial Charge Transfer and Separation for Photocatalytic NO Removal

Zhenyu Wang [a,b], Yu Huang [b,c*], Long Chen [b,c], Meijuan Chen [a], Junji Cao [a,b,c*], Wingkei Ho [d], Shun Cheng Lee [e]

Graphitic carbon nitride (g-C₃N₄) as a metal-free semiconductor photocatalyst is continually struggling with the high recombination rate of photo-induced charge carriers. Developing heterostructure is an effective way to suppress the photo-induced e⁻-h⁺ pairs recombination. In this study, a novel heterostructured g-C₃N₄/hierarchical reuleaux triangle LaCO₃OH nanocomposite was controllably fabricated via one-pot hydrothermal strategy for the first time rather than though the conventional solid state calcination reaction, relying on the dual-functional roles of g-C₃N₄. g-C₃N₄, serving as both structural direct agent and CO₃²⁻ source in the reaction system, significantly influence the morphology engineering of LaCO₃OH. The time-dependent structure evolutions were discussed in detail. The booming interfacial charge transfer and separation are the dominant factors for activity enhancement of g-C₃N₄/LaCO₃OH towards gaseous nitric oxide (NO) degradation under visible light, as confirmed by experimental characterizations and density functional theory (DFT) theoretical calculations. Combined with the identification of reaction intermediates and electron spin resonance (ESR) results, the photocatalytic degradation mechanism of NO over g-C₃N₄/LaCO₃OH heterojunction was proposed. More importantly, this novel self-sacrificial synthesis strategy was successfully extended to synthesize both g-C₃N₄/Bi₂O₂CO₃ and g-C₃N₄/SrCO₃ composites, indicating it can serve as a general method to synthesize g-C₃N₄/carbonate compounds.

1. Introduction

Nowadays, overwhelming attention is focused on visible-light sensitive photocatalysts due to the high efficiency for solar-energy utilization.[1-3] g-C₃N₄ as the first metal-free semiconductor has attracted attention in the environmental remediation field, relying on its visible-light response, stacking 2D graphite-like layered structure and low-cost of production.[4-6] The nanoarchitecture engineering,[7-9] elements doping,[10-13] and molecular copolymerization [14, 15] are considered as effective strategies for tuning the electronic band structure of pristine g-C₃N₄ to improve the visible-light catalytic performance, but these single-phase modified strategies are insufficient to restrain the recombination of photo-induced carriers efficiently. For the recombination process of charge carriers, the excited electrons revert to the valence band, dissipating the redundant energy as heat without joining in the photocatalysis reaction.[16] In contrast to single-phase engineering, g-C₃N₄-based heterostructure construction can effectively suppress the photoinduced e⁻-h⁺ pairs recombination by interface transfer and synergistic catalytic effects,[17] such as g-C₃N₄/TiO₂, g-C₃N₄/Bi₂O₂CO₃, g-C₃N₄/Ag₂O, g-C₃N₄/Bi₂WO₆, et al.[18-22]

Usually, hydro-/solvothermal strategy is considered as an important way to synthesize crystal materials, especially for composites, due to the merits in morphology control, crystal face growth rate adjustment and crystallinity improvement. However, most of the g-C₃N₄-based nanohybrids have to be prepared by solid-solid calcination method, rather than through hydrothermal strategy because g-C₃N₄ can generate impurity groups, CO₃²⁻ and NH₄⁺, by self-decomposition in hydrothermal reaction. This issue has built a barrier for extending g-C₃N₄-based composites due to some components obtained only by hydrothermal method or not tolerated quenching treatment. Nevertheless, it gives us an inspiration, whether this disadvantage of g-C₃N₄ can transform into a merit for g-C₃N₄/carbonate composites fabrication. In our recent work, the (001) faces exposed quadrate Bi₂O₂CO₃/g-C₃N₄ heterojunction was successfully prepared with the assistance of g-C₃N₄ self-sacrificing strategy for the first time.[20]

a School of Human Settlements and Civil Engineering, Xi'an Jiaotong University, Xi'an 710049, China
b Key Lab of Aerosol Chemistry & Physics, Institute of Earth Environment, Chinese Academy of Sciences, Xi'an 710061, China
c State Key Lab of Loess and Quaternary Geology (SKLLQG), Institute of Earth Environment, Chinese Academy of Sciences, Xi'an 710061, China
d Department of Science and Environmental Studies, The Hong Kong Institute of Education, Hong Kong, China
e Department of Civil and Environmental Engineering, The Hong Kong Polytechnic University, Hung Hom, Hong Kong, China
*Corresponding author:
Prof. Yu Huang, E-mail address: huangyu@ieecas.cn Tel: 86-29-6233 6261
Prof. Junji Cao, E-mail address: cao@loess.llqg.ac.cn
Electronic Supplementary Information (ESI) available: [details of any supplementary information available should be included here]. See DOI: 10.1039/x0xx00000x

LaCO₃OH, an important member of the rare-earth hydroxycarbonate family, has been prepared with different morphologies (apple-like structure, plum blossom-like structure, triangular heart structure, microspheres, nanowires, et al) [23-27] of luminescent property,[23, 26] and can also serve as a morphology-controlled template for the synthesis of La₂O₃ or La(OH)₃ in recent years.[28] Fascinatingly, LaCO₃OH possesses relatively negative conduction band and positive valence band edges, which ensures sufficient potential for photocatalytic hydrogen production and organic pollutants decomposition. In addition, the combination of narrow band gap semiconductors with the wide band gap LaCO₃OH to build heterojunction is expected to be an effective strategy for charges or holes accelerated separation because of the formation of built-in electric field at interfaces. In 2013, Pan et al. firstly reported LaCO₃OH as a photocatalyst exhibiting three times hydrogen evolution efficiency from aqueous methanol solutions than that of anatase TiO₂ under UV light irradiation.[29] Very recently, Patil et al. prepared graphene-wrapped Ag₃PO₄/LaCO₃OH heterostructures via the in-situ wet chemical method, exhibiting a superior photocatalytic activity for methylene blue degradation under visible-light irradiation.[30] Thus far, the application of LaCO₃OH in gas-phase pollutants degradation has not been reported.

In light of previous accomplishment, herein, a novel LaCO₃OH hierarchical reuleaux triangle nanostructure was tunably fabricated for the first time. During the hydrothermal process, g-C₃N₄ plays dual roles, CO₃²⁻ provider and structure-directing agent. Synergistic effects and intimate interfacial contact of g-C₃N₄/LaCO₃OH are the dominant factors for activity enhancement towards NO degradation under visible light, which was confirmed by the experimental characterizations and DFT theoretical calculation. More importantly, this novel synthesis strategy was successfully extended to synthesize both g-C₃N₄/Bi₂O₂CO₃ and g-C₃N₄/SrCO₃ composites, indicating it can serve as a general method to synthesize g-C₃N₄/carbonate compounds.

2. Experimental section

2.1 Synthesis of g-C₃N₄ sample

10 g of melamine powder was put into an alumina crucible with a cover, and then heated to 550 °C in a muffle furnace for 3h at a heating rate of 5 °C/ min. The resulted powder was collected for use without further treatment.

2.2 Synthesis of g-C₃N₄/LaCO₃OH heterojunction samples

All chemicals were used without further purification. g-C₃N₄/LaCO₃OH composites (CN-LCOH for short) were synthesized using a hydrothermal approach. In a typical process, 2.0 g of La(NO₃)₃·6H₂O was dispersed in 70 mL of deionized water and stirred for 30 min. Then, 0.9 g of g-C₃N₄ was added to the above solution. After 45 min of ultrasonic treatment, 0.625 M NaOH was added to adjust the pH to 8.0~8.5. The mixture was transferred into a 100 mL Teflon-lined autoclave and heated for 4, 8, or 12 h at 160 °C. After cooling down to room temperature naturally, the products were collected by filtration, washed thoroughly three times with deionized water and absolute ethanol alternately, dried at 60 °C for 12 h, and then labeled as CN-LCOH-4, CN-LCOH-8, and CN-LCOH, respectively. For comparison, Na₂CO₃ was used instead of

g-C₃N₄ to synthesize LaCO₃OH in the same manner at 160 °C for 12 h. Two parallel experiments of CN-LCOH were done and labeled as CN-LCOH-1 and CN-LCOH-2, respectively. Then, we changed the dosage of La(NO₃)₃·6H₂O from 1.5 to 2.5 g with 0.5 g increment and labeled as CN-LCOH-1.5, CN-LCOH, and CN-LCOH-2.5, respectively. The content of g-C₃N₄ and LaCO₃OH in g-C₃N₄/LaCO₃OH heterojunction was investigate by elemental analysis (Table S1) and optimized in term of photocatalytic activity. According to the results of photocatalytic activities evaluations (Figure S1), the CN-LCOH with 75.77% g-C₃N₄ and 24.23% LaCO₃OH was chosen as the research object because of the optimal photocatalytic activity. Based on the elemental analysis results, the nitrogen contents in g-C₃N₄ and CN-LCOH were 63.46% and 48.82%, respectively. Therefore, it can be deduced that the mass contents of g-C₃N₄ were estimated to be 75.77% in CN-LCOH. A mechanically mixed sample was prepared by the physical ultrasound method with 75.77% g-C₃N₄ and 24.23% LaCO₃OH. This procedure for preparation of g-C₃N₄/Bi₂O₂CO₃ and g-C₃N₄/SrCO₃ has been repeated using Bi(NO₃)₃·5H₂O and Sr(NO₃)₂, respectively.

2.3 Characterization

Scanning electron microscopy (SEM, JEOL JSM-6490, Japan) was used to characterize the morphology of the obtained products. Transmission electron microscopy (TEM) and EDX elemental mappings were performed using a JEOL JEM-2100HR CM-120 (Japan) transmission electron microscope. The crystal phase was analyzed via X-ray diffraction (XRD) with Cu Kα radiation at a scan rate of 0.05° 2ϑ/s (λ = 1.5406 Å, 40 kV, 40 mA, PANalytical X' Pert PRO X-ray diffractometer). Elemental analyses were carried out on a Elementar Vario EL instrument (Vario EL III, German, detection limit: 0.015%, standard deviation: ≤ 0.1% abs) with He purging for 20 s prior to testing. Samples were embedded in KBr pellets and then subjected to Fourier-transform infrared spectroscopy (FT-IR) on a FT-IR absorption spectrometer (Magna-IR 750, Nicolet, USA). X-ray photoelectron spectroscopy (XPS) was conducted using an X-ray photoelectron spectrometer (Thermo ESCALAB 250, USA). All binding energies were calibrated to the C 1s peak at 284.6 eV of the surface adventitious carbon. Moreover, a nitrogen adsorption apparatus (ASAP 2020, USA) was used to obtain the BET of the samples that were degassed at 250 °C prior to analysis. A Varian Cary 100 Scan UV-Visible system equipped with a labsphere diffuse reflectance accessory was used to obtain the reflectance spectra of the catalysts over a range of 200~800 nm. The intermediate and final products, nitrate and nitrite ions, were extracted by immersing the powders (about 0.05 g) into 6 mL deionized water and measured by using a Dionex-600 Ion Chromatograph (IC, Dionex Inc., Sunny-vale, CA, USA) after the photocatalytic activity test equipped with an IonPac AS14A column. The mobile phase was composed of a mixture of 1.8 mM Na₂CO₃ and 1.7 mM NaHCO₃ at a flow rate of 1.20 mL min⁻¹, the volume of samples was 20 μL. The detection limits for NO₂⁻ and NO₃⁻ are 0.0050 μg mL⁻¹ and 0.0256 μg mL⁻¹. The surface photovoltage (SPV) spectroscopy was conducted on a home-made detection system, which includes a source of monochromatic light provided by a 500 W xenon lamp and a double-prism monochromator, a lock-in amplifier (SR830-DSP) with a light chopper (SR540), a photovoltaic cell and a computer. The construction of photovoltaic cell was made by pressing the powder sample into two indium tin oxide (ITO) electrodes to form a

sandwich-like structure. The SPV signal was recorded in the wavelength range of 300 to 800 nm. Samples for electron spin-resonance spectroscopy (ESR, ER200-SRC, Bruker, Germany) were prepared by mixing 0.05 g of the as-prepared photocatalyst in a 25 mM 5,5'-dimethyl-1-pirroline-N-oxide (DMPO) solution with a 50 mL aqueous dispersion for DMPO-•OH or a 50 mL alcohol dispersion for DMPO-•O$_2^-$ under irradiation with 420 nm visible light.

2.4 Photocatalytic activity tests

The photocatalytic activities of the as-prepared samples were investigated in terms of NO removal at ppb levels in a continuous flow photocatalytic reactor system (Scheme S1) at an ambient temperature. The rectangular reactor, which was fabricated from stainless steel and covered with quartz glass, possessed a volume capacity of 4.5 L (30 cm × 15 cm × 10 cm). A 300 W commercial Xe arc lamp (microsolar 300, Perfectlight, China) was vertically placed outside the reactor. UV light in the light beam was removed by adopting a UV cutoff filter (420 nm). The photocatalyst (0.1 g) was coated onto one dish (10.0 cm in diameter), which was subsequently pretreated at 60 °C to remove water in the suspension. NO gas was supplied by a compressed gas cylinder at a concentration of 48 ppm (N$_2$ balance) in accordance with the standard of the National Institute of Standards and Technology. The initial NO concentration was diluted to 400 ppb by an air stream supplied by a zero-air generator (Model 1001, Sabio Instruments LLC, Georgetown, TX, USA), and the flow rate was controlled at 3 L/min. The lamp was turned on when the adsorption-desorption equilibrium was achieved and the optical power density reaching the sample surface was calibrated to be 25.46 mW/cm^2 (Thorlabs PM100D optical power meter). The concentration of NO was continuously measured using a chemiluminescence NO analyzer (Model 42c, Thermo Environmental Instruments Inc., Franklin, MA, USA). This apparatus was used to monitor NO and NO$_2$ concentrations at a sampling rate of 0.6 L/min. The removal ratio (η) of NO was calculated as η (%) = (1−C/C$_0$)×100, where C and C$_0$ are the concentrations of NO in the outlet and feeding streams, respectively.

2.5 Photoelectrochemical measurements

Photoelectrochemical properties of the as-prepared samples were evaluated using a Parstat 4000 electrochemical workstation (USA) in a conventional three-electrode cell, with a platinum plate and an Ag/AgCl electrode as the counter and reference electrodes, respectively. The photoelectrodes with geometric surface area of 1 cm^2 were exposed to periodic front-side illumination by a 420 nm LED The photocurrent-time curves were measured at 0.2 V versus Ag/AgCl in 0.5 mol/L Na$_2$SO$_3$ (pH 12) at an ambient temperature. For Mott-Schottky (M-S) measurement, the working electrode was immersed in 0.1 M Na$_2$SO$_4$ aqueous solution (pH 12), and subjected to 5 mV perturbation bias at fixed frequency of 1 kHz from -0.6 to 0.8 V vs. Ag/AgCl.

2.6 DFT Calculations

All the calculations were performed within the framework of the density functional theory (DFT) using a basis set consisting of plane waves, as implemented in the Cambridge Serial Total Energy Package (CASTEP).[31] The exchange-correlation energy and electron-ion interactions are calculated with the Perdew-Burke-Ernzerhof (PBE) [32] +U [33] formulation of the generalized gradient approximation

(GGA).[34] A plane-wave cut-off of 300 eV and 450 eV was used for LaCO$_3$OH and g-C$_3$N$_4$ calculations. The energy and residual force convergence criterion were set to 2.0e-5 eV/atom and 0.05 eV/Å for geometry optimization, respectively. We used 2×2×1 and 3×3×1 Monkhorst-pack k-point mesh for geometry optimization of the bulk LaCO$_3$OH and g-C$_3$N$_4$, and a 4×4×1 mesh to calculate their density of states (DOS). Also, we used a 2×2×1 Monkhorst-pack k-point mesh for geometry optimization of the LaCO$_3$OH/g-C$_3$N$_4$ composites, and a 4×4×1 mesh to calculate its DOS. Charge transfer was calculated by electron density difference (EDD) on the basis of the Miliken Population Analysis (MPA). [35]

3. Results and discussion

The bulk g-C$_3$N$_4$ obtained after drying from La(NO$_3$)$_3$ solution with layered structure (Figure 1a) and pure LaCO$_3$OH sheets (Figure 1b) with different sizes and irregular shapes are displayed by SEM. As shown in Figure 1c, the LaCO$_3$OH hierarchical self-assembly reuleaux triangle nanostructure with diameter about 10 μm implant into the irregular bulk g-C$_3$N$_4$. Furthermore, in HRTEM image of CN-LCOH (Figure 1d), amorphous g-C$_3$N$_4$ and (302) planes of hexagonal LaCO$_3$OH can be observed at the boundary, further suggesting the intimate interface contact between them. In order to examine the elemental distribution of the composite material, EDX elemental mapping images were recorded in Figures 1e−1i. The results indicate that N (magenta), C (yellow) and O (cyan) elements are distributed uniformly in the whole area, and the La (red) elements are distributed in the arc-shaped area, agreeing the SEM and TEM results.
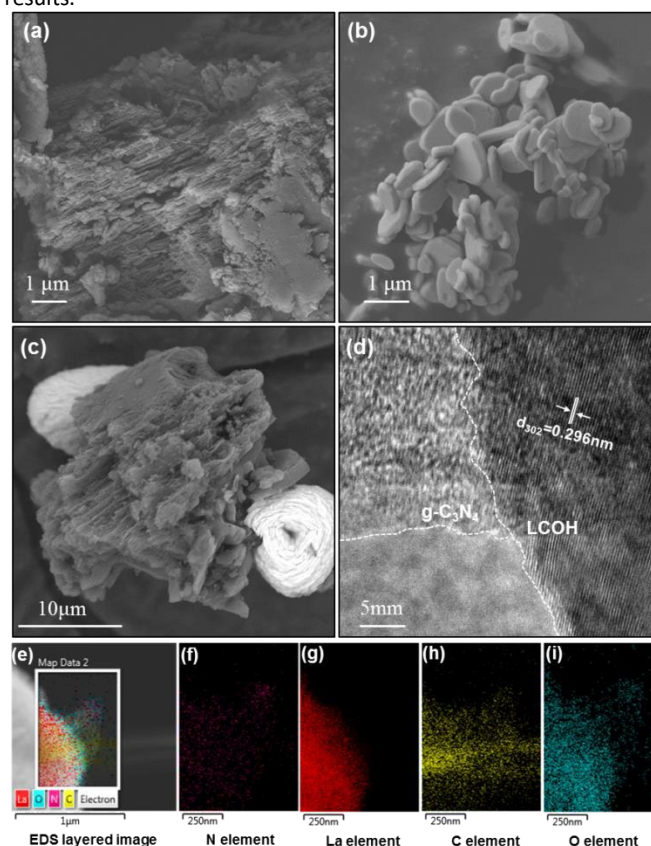

Figure 1. SEM images (a) of the g-C$_3$N$_4$ after drying from La(NO$_3$)$_3$ solution, (b) LaCO$_3$OH and (c) CN-LCOH at low magnification;

HRTEM image of CN-LCOH (d); EDX elemental mapping image (e), indicating the spatial distribution of N (f), La (g), C (h) and O (i), respectively.

The crystal structure and chemical composition information on all samples were evaluated using X-ray diffraction, elemental analyses and FT-IR analysis. Figure 2a shows the XRD patterns of the as-prepared LCOH, CN-LCOH, and CN samples. Apparently, the typical diffraction peaks of hexagonal (JCPDS NO. 26-0815) $LaCO_3OH$ [29] and g-C_3N_4 [4] can be observed in the CN-LCOH sample, demonstrating that g-C_3N_4/$LaCO_3OH$ composite has been successfully constructed by self-sacrificing parts of g-C_3N_4 as CO_3^{2-} provider. Based on the elemental analysis results (Table S1), the nitrogen contents in g-C_3N_4, CN-LCOH, CN-LCOH-1 and CN-LCOH-2 were 63.46%, 48.82%, 48.65%, and 48.53%, respectively. Therefore, it can be deduced that the mass contents of g-C_3N_4 were estimated to be 75.77%, 75.48%, and 75.30% in CN-LCOH, CN-LCOH-1 and CN-LCOH-2, respectively, implying the well reproducibility and controllability of this self-sacrificial synthesis strategy. The FT-IR spectra of the LCOH, CN-LCOH, and CN samples are shown in Figure 2b. For pure LCOH, four typical carbonate ion modes and stretching vibration of OH appear at 873 cm^{-1} (v_1), 843cm^{-1} (v_2), 1437~1498cm^{-1} (v_3), 705-776cm^{-1} (v_4), and 3615cm^{-1}, respectively.[26, 29] For pure CN, the intensive bands in the 1200~1700 cm^{-1} region indicate the stretching vibration of the heptazine heterocyclic ring (C_6N_7) units. The peaks at 807 cm^{-1} and 890 cm^{-1} are assigned to the breathing mode of the heptazine ring system and the deformation mode of N-H, respectively, and the broad band at 3400~3600 cm^{-1} is due to physically adsorbed H_2O.[7, 20] The CN-LCOH sample shows the characteristic absorption bands of both LCOH and CN, thereby confirming the co-presence of LCOH and CN components, which agrees with the aforementioned results. The surface chemical states and composition of as-prepared samples were further analyzed by XPS. The surveyed spectra in Figure S2a implies the presence of N, C, La, and O in the prepared nanocomposite sample. Figure S2b shows that the binding energies of La 3d$_{3/2}$ and La 3d$_{5/2}$ are 850.5 and 833.7 eV, and the shake-up peaks located at 838.8 and 855.3 eV correspond to the La (III)

oxidation state, respectively.[26, 36] The distinctive binding energy positive drifts observed in CN-LCOH can be attributed to the change in inner electron density caused by the formation of the g-C_3N_4/$LaCO_3OH$ heterojunction. In the C 1s region (Figure S2c), the sharp peak around 284.6 eV is assigned to adventitious carbon species from XPS measurement. The C 1s peak around 286.3, 288.2 eV in CN-LCOH and CN, and 289.5 eV in LCOH can be assigned to the C-NH/NH$_2$, sp^2-hybridized carbon in trizine rings, and the C-O peak, respectively.[26, 37, 38] In the N 1s region (Figure S2d), the main N 1s peak around the binding energy of 398.8 eV can be assigned to the sp^2 hybridized aromatic N bonded to carbon atoms (C=N–C), and the weak peak at 400.3 eV is attributed to the tertiary nitrogen N–(C)$_3$ groups or H–N–(C)$_2$ [38, 39] in both CN and CN-LCOH samples.

The textural and band gap structure on the obtained samples were evaluated by nitrogen adsorption measurement, UV-vis DRS and Mott-Schottky (M-S) measurement. The BET surface areas of LCOH, CN, mechanical mixture, and CN-LCOH were determined to be 6.2, 10.8, 17.5, and 33.2 m^2/g by nitrogen adsorption measurement, respectively. That is to say, the in situ fabrication $LaCO_3OH$ with hierarchical structure by g-C_3N_4 has larger specific surface area than the one by Na_2CO_3. Besides, UV-vis DRS results indicate that the light absorption edges of $LaCO_3OH$ and g-C_3N_4 are located at about 275 nm and 471 nm (Figure 2c), corresponding to the band gap of 4.50 eV and 2.63 eV, respectively, according to the Kubelka–Munk method.[40] In addition, M-S plots can be used to determine flat band potential of semiconductor. From the results in Figure 2d, both g-C_3N_4 and $LaCO_3OH$ are demonstrated to be the n-type semiconductor due to the positive slope of the linear plots,[41] and the flat band potentials (V_{fb}) of them are -1.33 and -1.15 V vs. Ag/AgCl at pH 7 (converted to -1.13 and -0.95 V vs. NHE at pH 7 through the Nernst equation).[42] For n-type semiconductor, the V_{fb} lies very close to the bottom of the conduction band (V_{CB}). Presumably, combined with V_{CB} and band gap results, the value band (V_{VB}) tops of g-C_3N_4 and $LaCO_3OH$ are calculated to be 1.50 V and 3.55 V, respectively. On the basis of the above data, the energy band structures of g-C_3N_4 and $LaCO_3OH$ can be staggered and have a potential to form Type II alignment,[17] as shown in Figure S3.
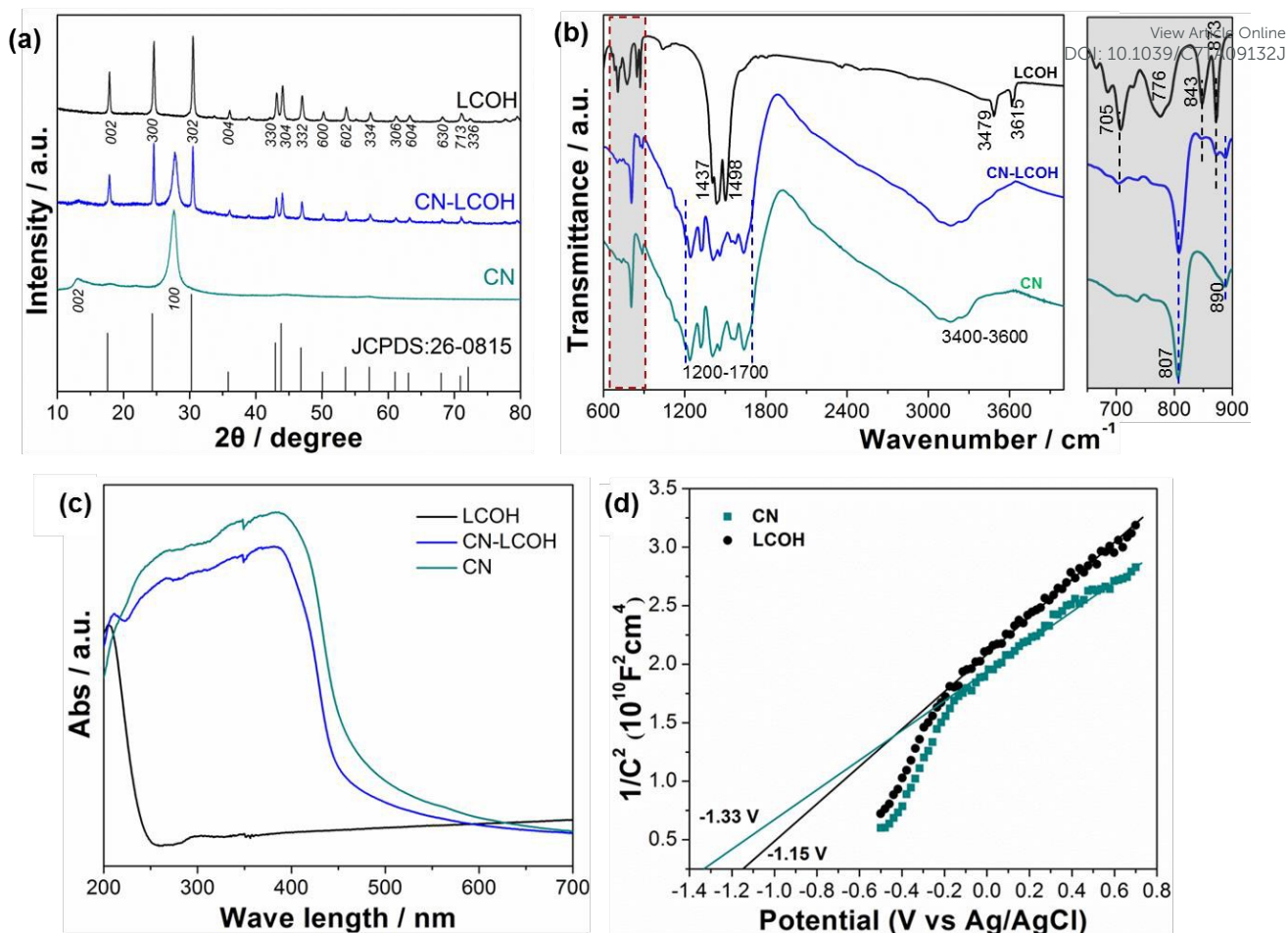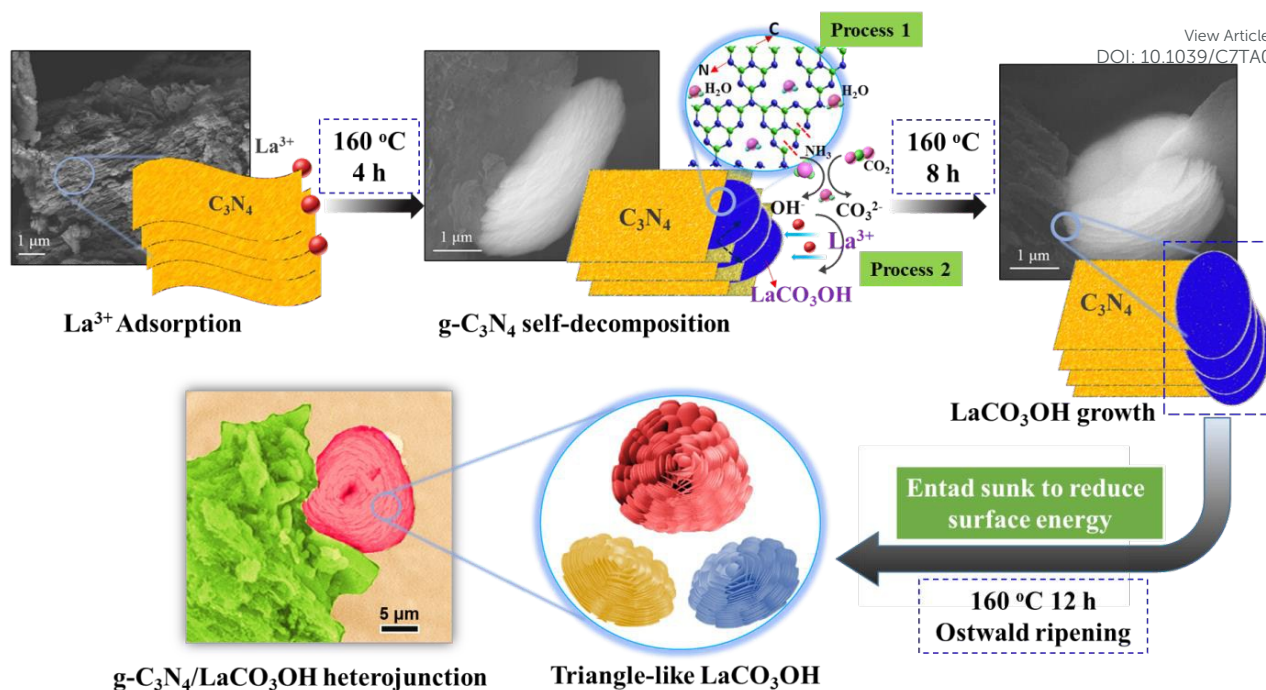
Figure 2. XRD patterns (a), FT-IR spectra (b) and UV–vis diffuse reflectance spectra (c) of pristine LCOH, CN-LCOH and CN, respectively; Mott-Schottky plots of LCOH and CN (d).

The g-C$_3$N$_4$/LaCO$_3$OH heterojunction formation pathways underlying time-dependent structure evolutions are shown in scheme 1. Simply, dual-function roles of g-C$_3$N$_4$: (1) one is a sacrificial agent to supply CO$_3$$^{2-}$. It can suffer from self-decomposition and generates CO$_3$$^{2-}$ and NH$_4$$^+$,[43, 44] similar to mesoporous silica SBA-15. Such a process can be considered disadvantageous for materials fabrication because of the impurity group introduced, but can be utilized to fabricate g-C$_3$N$_4$/carbonate composite (The generation of CO$_3$$^{2-}$ from the decomposition of g-C$_3$N$_4$ was proved by an experiment and details were shown in Figure. S4). The hydrolyzation process of the g-C$_3$N$_4$ released CO$_3$$^{2-}$ ions gradually by the tail C chin self-sacrifice due to the weaker binding energy (process 1 in scheme 1), which provided adsorption and growth sites for La^{3+} ions. (2) Another is a structure-directing agent to form layered LaCO$_3$OH nanosheets (process 2 in scheme 1). Briefly, The layer structure of g-C$_3$N$_4$ gradually decomposed along the layer direction and the La^{3+} combined with CO$_3$$^{2-}$ and OH$^-$ to form LaCO$_3$OH nanosheets along the g-C$_3$N$_4$ disappeared direction. With the time prolonged, the LaCO$_3$OH nanosheets become to larger hierarchical layer structure by uniform epitaxial growth due to the stably CO$_3$$^{2-}$ supply in the g-C$_3$N$_4$ self-sacrifice reaction system. As the treatment time was extended to 12 h, the hierarchical structure surface of LaCO$_3$OH entad sunk to reduce surface energy and the hierarchical curved edge triangle-like LaCO$_3$OH constructed by numerous nanoplatelets was obtained eventually by Ostwald ripening. The growth pattern of LaCO$_3$OH is different from the alkali system replaced g-C$_3$N$_4$ by Na$_2$CO$_3$. Random sizes polygon nanosheets of pure LaCO$_3$OH can be formed due to lack of structure-directing and stably CO$_3$$^{2-}$ concentration (Figure 1b). It is believed that the structural direct and CO$_3$$^{2-}$ supply pattern in the reaction system has a vital influence on the morphology of LaCO$_3$OH.

Scheme 1. Schematic illustration of the synthesis process of g-C$_3$N$_4$/LaCO$_3$OH heterojunctions.

The as-prepared LCOH, CN-LCOH, and CN samples were employed in the photocatalytic removal of NO under visible-light irradiation in a continuous reactor to demonstrate their potential capability in air purification, as shown in Figure 3a. The dynamic adsorption/desorption equilibrium of NO over all the samples in dark was achieved before opening the light source and the direct photolysis of NO without photocatalyst under visible-light irradiation was excluded by controlled experiments. The pristine LaCO$_3$OH has no photocatalytic activity under visible-light because of the large band gap. The removal ratios of NO by pristine CN and CN-LCOH composite are 19.3% and 30.3% after 30 min of visible-light irradiation, respectively. In order to evaluate the effect of hydrothermal treatment on photocatalytic NO removal, the photocatalytic activity of CN after hydrothermal treatment without other additive is evaluated. From Figure S5, it is found that hydrothermal treatment of CN has ignorable effect towards photocatalytic NO removal. These results suggest that photocatalytic activity was enhanced by the heterostructure fabrication. For comparison, we calculate the content ratio of CN and LCOH in CN-LCOH sample and mixed two pure phases proportionally by the physical ultrasound method. The photocatalytic activity of the mechanically mixed sample (25.2%) is 5.1% lower than that of CN-LCOH heterojunction under the same condition, indicating the importance of synergy effects by the in-situ interfacial connection.[45] The reaction intermediate NO$_2$, produced during photocatalytic oxidation of NO, can hinder for NO degradation and the photocatalyst application because of active sites occupied and its toxicity. Thus, the by-product of NO$_2$ is monitored online (Figure S6a) and selectivity is calculated (Details about NO$_2$ selectivity is given in the ESI†). The results show CN-LCOH displays the lowest conversion ratio (11.6%) of NO to NO$_2$ than CN (39.5%) and mechanical mixture sample (40.4%), as shown in Figure S6b. Above results imply that the CN-LCOH heterojunction has better potential capability in air purification because of

outstanding performance to prefer the transformation from gas phase NO to particle phase nitrate, rather than toxic NO$_2$. The accumulated products on the surface of the CN-LCOH sample after single run reaction were extracted by deionized water and measured by the ion chromatography (IC) method. It was found that the amounts of NO$_3^-$ and NO$_2^-$ accumulated on the CN-LCOH surface were 12.30 μmol and 0.01 μmol, which indicated that the oxidation of NO to NO$_3^-$ was the major conversion process. Multiple cycles of repeated experiments over the CN-LCOH were carried out to further test the stability on photocatalytic NO removal. After undergoing five repeated runs, the NO removal ratio of CN-LCOH heterojunction remains high, and FT-IR spectra (Figure S7) of recyclable sample are almost identical to the fresh sample, suggesting the excellent phase stability and performance stability of CN-LCOH. Certainly, the superior photocatalytic activity can be mainly attributed to the effective charge carriers migration and separation ability.

To understand the heterojunction effect on the photocatalytic activity enhancement, transient photocurrent response and surface photovoltage (SPV) spectroscopy measurements were implemented to investigate the photoinduced charge transfer behaviors of obtained samples. Firstly, as shown in Figure 3b, all the samples exhibit prompt photocurrent signals with a reproducible response to on/off cycles and the density generated by CN-LCOH heterojunction (1.2 μA/cm^2) is 2.4, 4, and 12 times higher than those of mechanically mixed sample (0.5 μA/cm^2), CN (0.3 μA/cm^2), and LCOH (0.1 μA/cm^2), respectively. In addition, the SPV respond owing to the incident wavelength meticulously reveals the photoinduced charges separation behaviors within different wavelength range. Figure. 3c shows the SPV spectra in which the response intensity was significantly strengthened in CN-LCOH heterojunction, again indicating the improved separation of photoinduced e$^-$-h$^+$ pairs in the in-situ heterojunction structure. More importantly, the SPV signal of CN-LCOH in the visible-light

region (~420 nm) is increased compared to that of CN, which means the high e⁻-h⁺ pairs separation rate may be attributed to the transfer of photo-generated electrons from g-C₃N₄ to LaCO₃OH. Mechanical mixture shows a weaker SPV signal than that of the *in-situ* heterojunction due to the lack of intimate interfaces.

To further examine the interaction, especially the charge carriers transfer direction, between g-C₃N₄ (Figure S8a) and LaCO₃OH (Figure S8b) at interfaces, a theoretical model was built by matching the respective preferential crystal face, (001) and (001) lattice planes for g-C₃N₄ and LaCO₃OH, respectively. Figure S8c shows the pristine structure of the g-C₃N₄ (001)/LaCO₃OH (001)

interface, and the geometry optimization result is shown in Figure S8d. The different degree deformation occurs at two interfaces due to the band structure re-arrangement. To explore how the charge transfer between g-C₃N₄ and LaCO₃OH, the charge density difference was calculated as shown in Figure 3d and the results shown that the charge transfer from g-C₃N₄ to LaCO₃OH is about 1.14 electrons across the interface. So, we conclude that the poor photocatalytic activity of g-C₃N₄ is primarily due to its inferior electric properties, but coupled with LaCO₃OH can promote interfacial charge effective separation, especially by in-situ growth method.
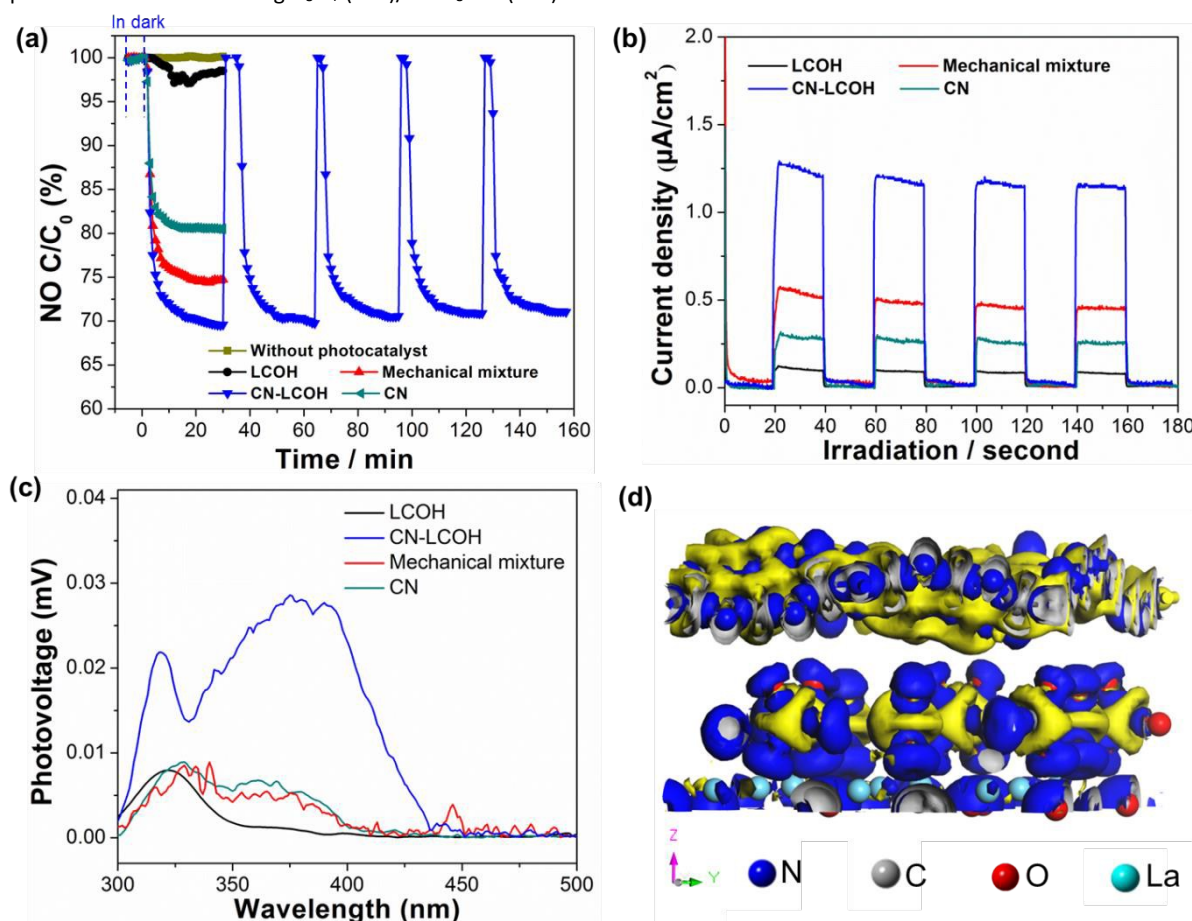

Figure 3. (a) Visible-light photocatalytic activities of LCOH, CN, Mechanical mixture, and cycling runs over CN-LCOH for NO removal in air; (b) Photocurrent transient under visible light irradiation (λ > 420 nm); (c) Surface photovoltage (SPV) spectra; (d) the calculated electron density difference (EDD) diagram of CN-LCOH (blue and yellow areas represent the increase and decrease of electron density, respectively).

According to above experiment and calculation results, it is concluded that the energy level difference forming built-in electric field between g-C₃N₄ and LaCO₃OH is the driving force to cause the electron-holes effective separation. Based on the above characterizations and analyses, the in-situ fabricated g-C₃N₄/LaCO₃OH heterojunction exhibiting superior visible-light-driven photocatalytic activity for NOx photocatalytic oxidation mechanism is proposed. Firstly, g-C₃N₄ can be excited by visible light and generate photo-induced electrons and holes, but LaCO₃OH cannot be subjected to identical conditions (process 1 in Figure 4a). The excited electron can transfer from g-C₃N₄ to LaCO₃OH because of the electric field force and interfacial contact (process 2). Secondly, compared with the mechanically mixed sample, CN-LCOH

possesses the hierarchical layered structure of LaCO₃OH, which can favor NO adsorption and intermediates diffusion. More importantly, upward or downward band bending can be created at the intimate interface to balance the Femi energy level due to the in-situ fabrication strategy, which can significantly ameliorate the charge migration and separation than that of mechanically mixed one.[46] Finally, the excited electrons are trapped by O₂ in the surrounding air to form reactive •O₂⁻ (process 3) and •OH radicals generated via the •O₂⁻→H₂O₂→•OH route (process 4) . The E$_{VB}$ of g-C₃N₄ (1.50 eV) is lower than the standard redox potential of H₂O/•OH (2.37 eV) but is higher than that of HNO₃/NO (0.94 eV), indicating that the photogenerated holes of g-C₃N₄ could not oxidize H₂O to active species •OH but may oxidize NO,[22] which are agreed with the

DMPO-ESR spin-trapping results. As shown in Fig. 4b, four apparent signals of $\bullet O_2^-$ were generated under visible-light irradiation and DMPO-$\bullet$OH adduct signals (Fig. 4c) are weaker than DMPO-$\bullet O_2^-$ signals, which confirm that $\bullet O_2^-$ is the dominant active species and $\bullet$OH radicals perform a minor function.[11] NOx reacts with the

photo-generated $\bullet O_2^-$, $\bullet$OH and h[+], and then NO_2^-, NO_3^- ions are produced (process 5-6), as the IC results. The related mechanisms for NO removal and photocatalytic activity enhancement over g-C_3N_4/$LaCO_3OH$ heterojunction are proposed accordingly as illustrated in Figure 4a.
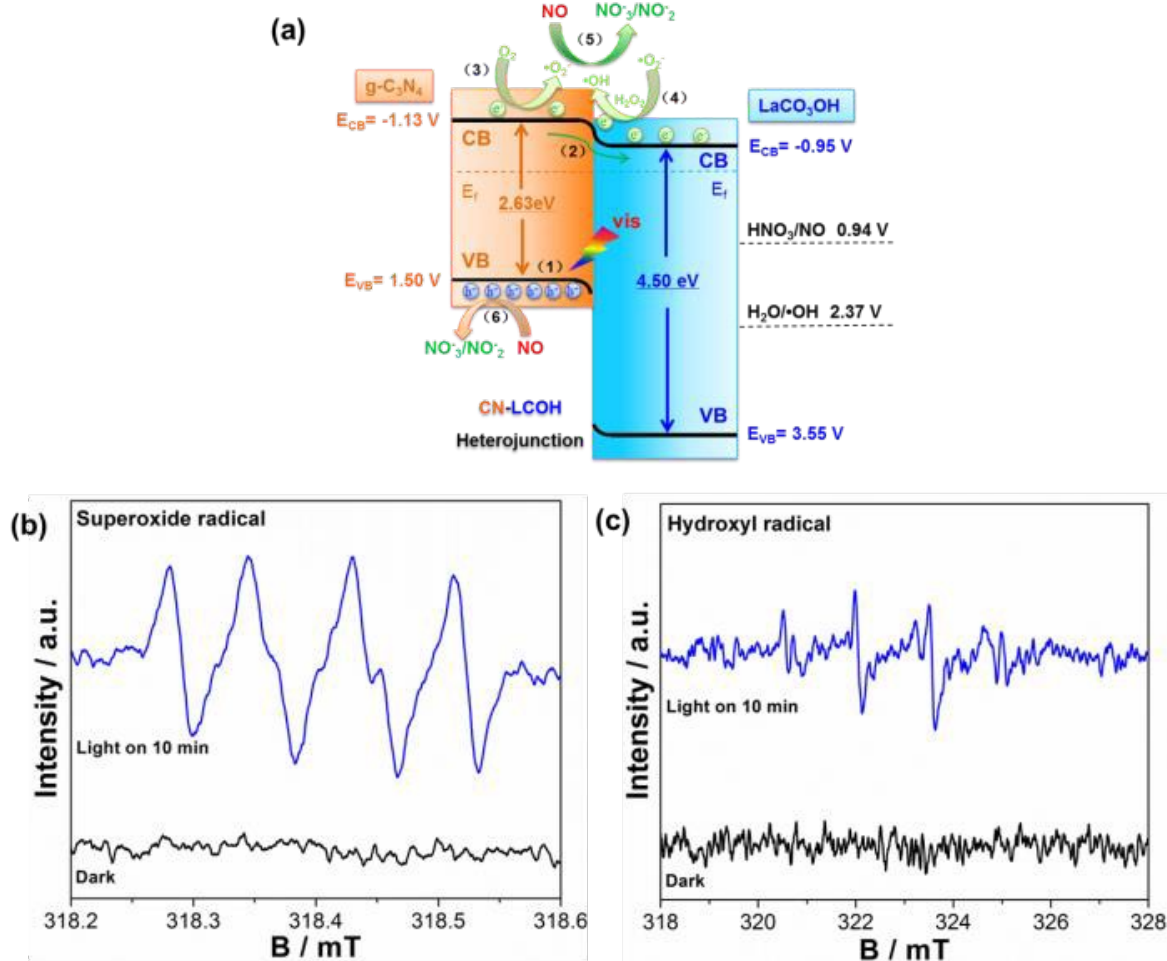

Figure 4. (a) Proposed photocatalytic mechanism for enhancing photocatalytic activity over g-C_3N_4/$LaCO_3OH$ heterojunctions for NO degradation under visible light irradiation; (b) DMPO spin-trapping ESR spectra of CN-LCOH in methanol dispersion for DMPO-$\bullet O_2^-$ and (c) in aqueous dispersion for DMPO-$\bullet$OH.

In order to explore whether the g-C_3N_4 self-sacrifice method is applicable to fabricate other g-C_3N_4 based carbonate composites, we change metal salt types as the comparative experiments and remain other reaction conditions unchanged. Wherein, $Bi(NO_3)_3$ and $Sr(NO_3)_2$ were chosen to replace $La(NO_3)_3$. Then, g-C_3N_4/$Bi_2O_2CO_3$ nanohybrid was prepared using $Bi(NO_3)_3$ as the precursor, in which many quadrate tetragonal $Bi_2O_2CO_3$ [47] (JCPDS NO. 41-1488, Figure S9a and Figure S10a) anchor on the bulk g-C_3N_4, as shown in Figure 5a. The elemental mapping images (Figures 5b–e) indicate that N, Bi and C are distributed on the obtained composite. What's more, the bulk g-C_3N_4/rod-cluster-like orthorhombic $SrCO_3$ [48, 49] (JCPDS NO. 05-0418, Figure S10b) composite can be fabricated when $Sr(NO_3)_2$ was

used as the precursor, which can be verified by XRD in Figure S9b and SEM in Figure. 5f. The elemental mapping images (Figures. 5g–j) indicate indicate that N, Sr and C are distributed on the obtained composite. The extra C elements in both samples are attributed to the signal from carbon film on the base grid. The removal ratios of NO over g-C_3N_4/$Bi_2O_2CO_3$ and g-C_3N_4/$SrCO_3$ composite are 33.5% and 25.5%, respectively, after 30 min of visible-light irradiation (Figure S11), which is higher than that of pristine g-C_3N_4. The aforesaid results sufficiently demonstrate that this novel synthesis strategy has unique merits for g-C_3N_4-based carbonate composites fabrication.
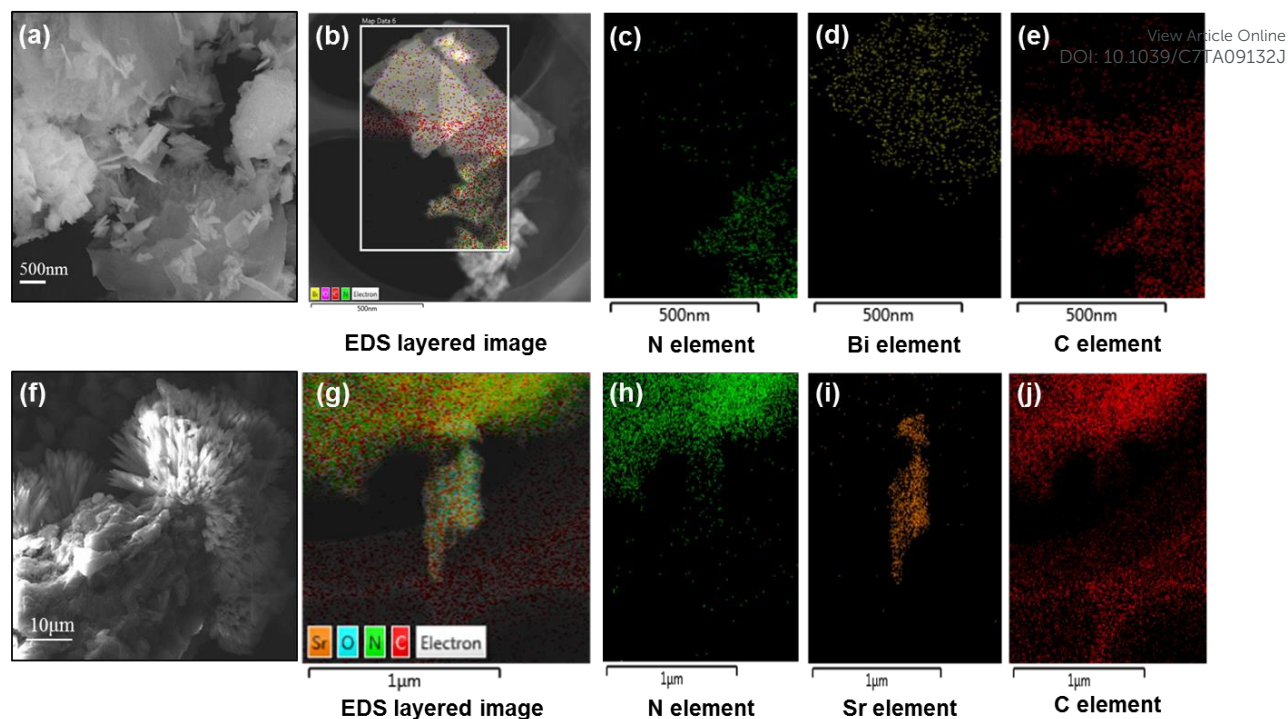
Figure 5. SEM images of g-C₃N₄/Bi₂O₂CO₃ (a) and g-C₃N₄/SrCO₃ (f) at low magnification; EDS elemental mapping image (b) and (g), indicating the spatial distribution of N (c) and (h), Bi (d), Sr (i), and C (e) and (j), respectively.

4. Conclusions

In summary, a novel heterostructured g-C₃N₄/LaCO₃OH nanocomposite was controllably fabricated via an one-pot hydrothermal strategy for the first time, relying on the dual-functional roles of g-C₃N₄, namely as a CO_3^{2-} provider and also as a structure-directing agent. Heterojunction formation pathways underlying time-dependent structure evolutions were discussed in detail. Synergistic effects and intimate interfacial contact of CN-LCOH can be considered as the main reasons for activity enhancement towards NO visible-light degradation due to the more effective interfacial charge separation efficiency. Both NO photocatalytic degradation and activity enhancement mechanisms over g-C₃N₄/LaCO₃OH heterojunction were proposed. More importantly, this novel synthesis strategy was successfully extended to synthesize g-C₃N₄/Bi₂O₂CO₃ and g-C₃N₄/SrCO₃ composites, respectively, indicating it can serve as a general method to synthesize g-C₃N₄/carbonate compounds heterojunctions.

Conflicts of interest

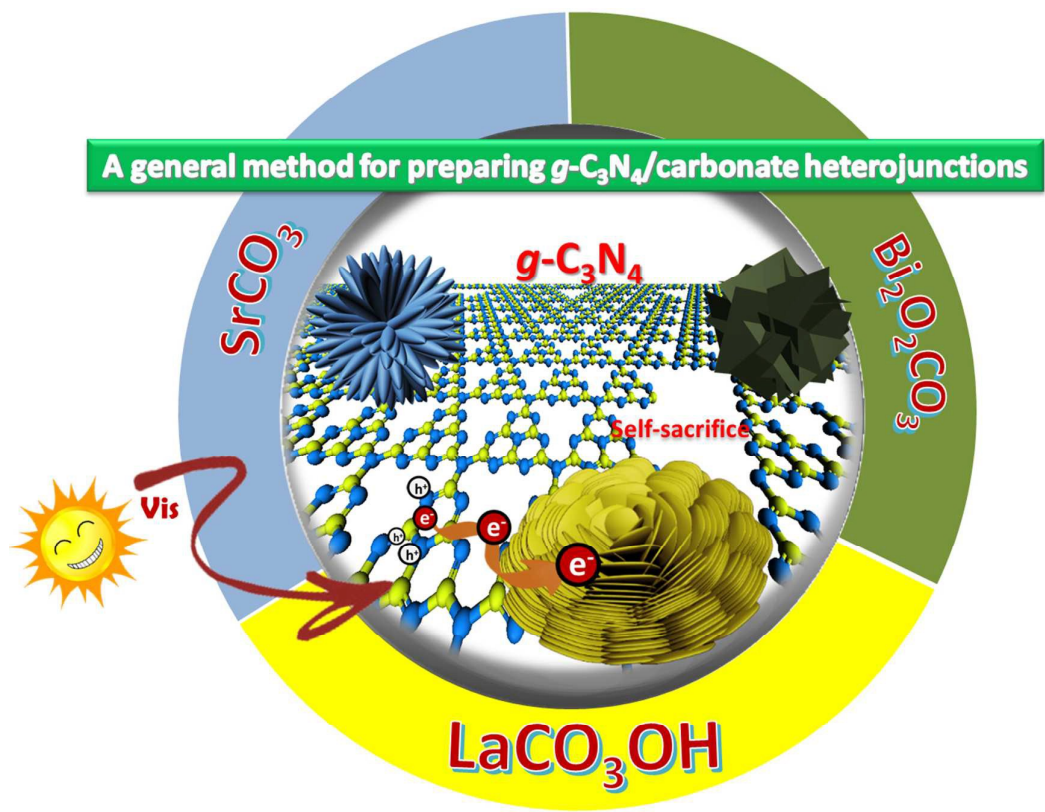The authors declare no conflicts of interest.

Acknowledgements

References

1 M. Pelaez, N. T. Nolan, S. C. Pillai, M. K. Seery, P. Falaras, A. G. Kontos, P. S. Dunlop, J. W. Hamilton, J. A. Byrne, K. O'shea, *Appl. Catal. B: Environ.*, 2012 **125,** 331-349.

2 Y. Wang, Q. Wang, X. Zhan, F. Wang, M. Safdar, J. He, *Nanoscale*, 2013 **5,** 8326-8339.

3 S. J. Moniz, S. A. Shevlin, D. J. Martin, Z.-X. Guo, J. Tang, *Energy Environ. Sci.*, 2015 **8,** 731-759.

4 X. Wang, K. Maeda, A. Thomas, K. Takanabe, G. Xin, J. M. Carlsson, K. Domen, M. Antonietti, *Nat. Mater.*, 2009 **8,** 76-80.

5 Y. Wang, X. Wang, M. Antonietti, *Angew. Chem. Int. Edit.*, 2012 **51,** 68-89.

6 J. Zhang, Y. Chen, X. Wang, *Energy Environ. Sci.*, 2015 **8,** 3092-3108.

7 Z. Wang, W. Guan, Y. Sun, F. Dong, Y. Zhou, W.-K. Ho, *Nanoscale*, 2015 **7,** 2471-2479.

8 J. Zhang, F. Guo, X. Wang, *Adv. Funct. Mater.*, 2013 **23,** 3008-3014.

9 J. Zhang, M. Zhang, C. Yang, X. Wang, *Adv. Mater.*, 2014 **26,** 4121-4126.

10 Y. Zhang, T. Mori, J. Ye, M. Antonietti, *J. Am. Chem. Soc.*, 2010 **132,** 6294-6295.

11 M. Zhang, X. Bai, D. Liu, J. Wang, Y. Zhu, *Appl. Catal. B: Environ.*, 2015 **164,** 77-81.

12 W. Cui; J. Li; W. Cen; Y. Sun; S. Lee; F. Dong, *J. Catal.,* 2017, ***352***, 351-360.

13 J. Li; W. Cui; Y. Sun; Y. Chu; W. Cen; F. Dong, *J. Mater. Chem. A*, 2017**, 5,** 9358-9364.

14 L. Ge, C. Han, J. Liu, *J. Mater. Chem.*, 2012 **22,** 11843-11850.

15 J. Zhang, X. Chen, K. Takanabe, K. Maeda, K. Domen, J. D. Epping, X. Fu, M. Antonietti, X. Wang, *Angew. Chem. Int. Edit.*, 2010 **49,** 441-444.

16 B. Liu, E. S. Aydil, *Chem. Commun.*, 2011 **47,** 9507-9509.

17 W.-J. Ong, L.-L. Tan, Y. H. Ng, S.-T. Yong, S.-P. Chai, *Chem. Rev*, 2016 **116,** 7159-7329.

18 J. Ma, C. Wang, H. He, *Appl. Catal. B: Environ.*, 2016 **184,** 28-34.

19 Y. Li, J. Wang, Y. Yang, Y. Zhang, D. He, Q. An, G. Cao, *J. Hazard. Mater.*, 2015 **292,** 79-89.

20 Z. Wang, Y. Huang, W. Ho, J. Cao, Z. Shen, S. C. Lee, *Appl. Catal. B: Environ.*, 2016 **199,** 123-133.

21 M. Xu, L. Han, S. Dong, *ACS Appl. Mater. Interfaces*, 2013 **5,** 12533-12540.

22 L. Ge, C. Han, J. Liu, *Appl. Catal. B: Environ.*, 2011 **108,** 100-107.

23 S.-L. Zhong, L.-F. Zhang, J.-W. Jiang, Y.-H. Lv, R. Xu, A.-W. Xu, S.-P. Wang, *CrystEngComm*, 2011 **13,** 4151-4160.

24 X. Yang, Z. Zhai, L. Xu, M. Li, Y. Zhang, W. Hou, *RSC Adv.*, 2013 **3,** 3907-3916.

25 Y.-X. Zhang, X.-B. Zhou, Z.-L. Liu, Q.-Z. Liu, G.-P. Zhu, K. Dai, B. Li, B. Sun, Z. Jin, X.-H. Li, *RSC Adv.*, 2015 **5,** 21925-21930.

26 Y. Zhang, K. Han, T. Cheng, Z. Fang, *Inorg. Chem.*, 2007 **46,** 4713-4717.

27 Z. Li, J. Zhang, J. Du, H. Gao, Y. Gao, T. Mu, B. Han, *Mater. Lett.*, 2005 **59,** 963-965.

28 J. Xie, Q. Wu, D. Zhang, Y. Ding, *Cryst. Growth. Des.*, 2009 **9,** 3889-3897.

29 B. Pan, Q. Xie, H. Wang, J. Zhu, Y. Zhang, W. Su, X. Wang, *J. Mater. Chem. A*, 2013 **1,** 6629-6634.

30 S. S. Patil, M. G. Mali, A. Roy, M. S. Tamboli, V. G. Deonikar, D. R. Patil, M. V. Kulkarni, S. S. Al-Deyab, S. S. Yoon, S. S. Kolekar, *Journal of Energy Chemistry*, 2016 **25,** 845-853.

31 M. Segall, P. J. Lindan, M. a. Probert, C. Pickard, P. Hasnip, S. Clark, M. Payne, *J. Phys.: Condensed Matter*, 2002 **14,** 2717.

32 J. P. Perdew, K. Burke, M. Ernzerhof, *Phys. Rev. Lett*, 1996 **77,** 1.

33 S. Dudarev, G. Botton, S. Savrasov, C. Humphreys, A. Sutton, *Phys. Rev. B*, 1998 **57,** 1505.

34 R. Parr, W. Yang, *Press, New York*, 1989.

35 R. S. Mulliken, *J. Chem. Phys.*, 1955 **23,** 1833-1840.

36 T.-D. Nguyen, C.-T. Dinh, T.-O. Do, *Inorg. Chem.*, 2011 **50,** 1309-1320.

37 Q. Lin, L. Li, S. Liang, M. Liu, J. Bi, L. Wu, *Appl. Catal. B: Environ.*, 2015 **163,** 135-142.

38 F. Dong, Z. Wang, Y. Li, W.-K. Ho, S. Lee, *Environ. Sci. Technol.*, 2014 **48,** 10345-10353.

39 B. Long, J. Lin, X. Wang, *J. Mater. Chem. A*, 2014 **2,** 2942-2951.

40 N. Serpone, D. Lawless, R. Khairutdinov, *J. Phys. Chem.*, 1995 **99,** 16646-16654.

41 L. Kavan, M. Grätzel, S. Gilbert, C. Klemenz, H. Scheel, *J. Am. Chem. Soc.*, 1996 **118,** 6716-6723.

42 M. Zhou, J. Bao, Y. Xu, J. Zhang, J. Xie, M. Guan, C. Wang, L. Wen, Y. Lei, Y. Xie, *ACS Nano*, 2014 **8,** 7088-7098.

43 Y.-S. Xu, W.-D. Zhang, *Appl. Catal. B: Environ.*, 2013 **140,** 306-316.

44 Y. J. Pagán-Torres, J. M. R. Gallo, D. Wang, H. N. Pham, J. A. Libera, C. L. Marshall, J. W. Elam, A. K. Datye, J. A. Dumesic, *ACS Catal.*, 2011 **1,** 1234-1245.

45 J. Shi, *Chem. Rev.*, 2012 **113,** 2139-2181.

46 H. Wang, L. Zhang, Z. Chen, J. Hu, S. Li, Z. Wang, J. Liu, X. Wang, *Chem. Soc. Rev.*, 2014 **43,** 5234-5244.

47 Y. Liu, Z. Wang, B. Huang, K. Yang, X. Zhang, X. Qin, Y. Dai, *Appl. Surf. Sci.*, 2010 **257,** 172-175.

48 W.-S. Wang, L. Zhen, C.-Y. Xu, L. Yang, W.-Z. Shao, Cryst. Growth Des., 2008 **8**, 1734-1740.

49 W. Cui; J. Li; F. Dong; Y. Sun; G. Jiang; W. Cen; S. C. Lee; Z. Wu, *Environ. Sci. Technol.,* 2017**, 51**, 10682-10690.

Journal of Materials Chemistry A Accepted Manuscript

For Table of Contents Only

The novel g-C$_3$N$_4$/LaCO$_3$OH heterojunction was controllably fabricated via *in-situ* self-sacrificial strategy and this strategy was extended to synthesize g-C$_3$N$_4$/carbonate compounds.